Local Atomic Structure of Partially Ordered NiMn in NiMn/NiFe Exchange Coupled Layers: 1. XAFS Measurements and Structural Refinement

Francisco J. Espinosa-Faller,[†,||] Rafael C. Howell,[†] Angel J. Garcia-Adeva,[†,⊥] Steven D. Conradson,*[,†] Alexander Y. Ignatov,[‡] Trevor A. Tyson,[‡] Robin F. C. Farrow,[§] and Michael F. Toney[§,#]

Materials Science and Technology Division, Los Alamos National Laboratory, Los Alamos, New Mexico 87545, Physics Deptartment, New Jersey Institute of Technology, Newark, New Jersey 07102, and IBM Almaden Research Center, 650 Harry Road, San Jose, California 95120-6099

Received: November 12, 2003; In Final Form: March 1, 2005

The local atomic structure of the Mn in NiMn/NiFe exchange coupled films was investigated using Mn *K*-edge extended X-ray absorption fine structure (EXAFS) measurements to elucidate the possible correlation between the coercivity that can occur even in samples that display no signs of NiMn $L1_0$ ordering in diffraction patterns and such ordering on a length scale below the diffraction limit. Raising the substrate growth temperature from 3 to 200 °C increases the extent of $L1_0$ ordering in the NiMn pinning layer and the associated coercivity. A short-range order parameter (S_{SRO}) was derived from EXAFS data for comparison with the long-range order parameter (S_{LRO}) obtained from the X-ray diffraction measurements. Analogous to S_{LRO}, S_{SRO} increases in tandem with the pinning layer coercivity, implying the presence of nanometer-scale ordered clusters at the beginning stages of macroscopic $L1_0$ phase formation that apparently foster antiferromagnetism despite their small size. The behavior of the EXAFS, especially the contributions of the more distant shells, also suggests that the overall structure in materials that are not fully $L1_0$-ordered is more accurately described as locally ordered, magnetically ordered, incoherent nanodomains of the $L1_0$ phase separated by locally disordered, strained, interdomain regions that globally average to the fcc lattice with little or no local fcc structure present. The constraints on the sizes and other characteristics of these domains were explored by examining the diffraction patterns calculated for several two-dimensional analogue structures. These demonstrated that one of the most important structural features in the development of a two-phase diffraction pattern was the presence of dislocations in response to the elastic strain at the interfaces between domains where the accumulated expitaxial mismatch was greater than half of the bond length that rendered the domains incoherent with respect to each other.

Introduction to the Series

Understanding and controlling the properties of complex materials, that is, those that exhibit complicated correlated or transformational behaviors when a small number of external parameters change (impurity concentration, temperature, pressure, etc.), are still at the forefront of condensed matter physics and material science. Examples include cuprate superconductors, manganite collosal magnetoresistance (CMR) compounds, martensites, and many alloys and other solid solutions. It is becoming increasingly accepted that the interesting, and oftentimes surprising, properties of these systems are related to scenarios in which phase separation, or at least the formation of two or more distinct structures with domain sizes below the diffraction limit, and resultant nanoscale heterogeneity occur. For example, in cuprate superconductors, holes arrange themselves into stripes where they can move without disrupting the long-range magnetic order, effectively giving rise to a separation between regions with magnetic order and regions rich in electrical charges.[1] Similarly, in CMR compounds, charge inhomogeneities several unit cells in extent competing with ferromagnetism are believed to be the origin of the CMR effect.[2] Moreover, in the case of substitutional impurities in solid solutions, if the impurities attract or repel each other, texture in the form of heterogeneous nanoscale domains may form in response to local composition fluctuations and strain that can result in anomalous lattice changes or complicated phase diagrams below the percolation limit.[3] Accepting these ideas poses the challenge of abandoning traditional interpretative frameworks and searching for new experimental probes, theories, and simulation methods.

In the present work, we undertake a comprehensive study of the structural and electronic/magnetic properties of Ni_xMn_{1-x} alloy films, a system that falls into the complex materials category. The magnetic and structural properties of Ni_xMn_{1-x} alloy films near the equiatomic composition $x = 0.5$ have generated interest both from the applied and basic viewpoints. An essential feature is that such films undergo long-range, crystallographic ordering from a chemically disordered fcc structure into a chemically ordered, $L1_0$ tetragonal phase which

* Author to whom correspondence should be addressed. E-mail: conradson@lanl.gov.
† Los Alamos National Laboratory.
‡ New Jersey Institute of Technology.
§ IBM Almaden Research Center.
|| Current affiliation: Centro Marista de Estudios Superiores, Periférico Norte Tablaje 13941, Mérida, Yucatán, México.
⊥ Current affiliation: Departmento Fisica Aplicada I, Escuela Superior de Ingenieros de Bilbao, Alda. Urquijo s/n, 48013 Bilbao, Spain.
Current affiliation: Stanford Linear Accelerator Center, Stanford University, Stanford, CA 94305.

10.1021/jp037449+ CCC: $30.25 © 2005 American Chemical Society
Published on Web 04/29/2005

comprises alternating atomic planes of Ni and Mn along the *c*-axis concomitant with a 1.5% contraction perpendicular to these planes.[4] In its chemically ordered state, NiMn is a strong antiferromagnet, which makes chemically ordered NiMn a good candidate for use as the exchange coupling material to pin the reference ferromagnetic layer in spin valve magnetic read sensors.[5,6] As has been shown, chemically ordered NiMn is capable of providing strong pinning fields, a high blocking temperature, thermal stability, and good corrosion resistance.[7−11] However, the scientific issue of understanding the evolution of the remnant coercitivity with the degree of chemical order (amount of $L1_0$) prior to full $L1_0$ development is not trivial. In fact, for the films analyzed in this work, this quantity is nonzero even for films where diffraction patterns exhibit no sign of the $L1_0$ phase. As we will show, this apparent contradiction is reconciled by nonclassical phase separation, perhaps better described as structural hetereogeneity in the sense that the arrangement of atoms and resultant properties are best described with a model consisting of two, coexisting, ordered structures with domain sizes below the diffraction limit that originate in the degree of local chemical ordering of the NiMn. That is, chemical order exists in the form of small nanoscale $L1_0$ domains immersed in a chemically disordered matrix (or nanoscale domains of one structure associated with mesoscale ones of the other) with an average, crystallographic fcc structure. These domains do not diffract well because they are too small and are organized in such a way that their only contribution to the diffraction patterns is in the form of smooth and very small contributions to the diffuse scattering component (see ref 12 for examples of distorted lattices where these types of effects occur). In addition, on this length scale, the elastic relaxation length is comparable to the domain size so that there is a continuum of interatomic distances that nevertheless allows all of the atoms to be classed into one of the two end point structures.

Within this structural heterogeneity on the nanoscale scenario, the obvious questions are the following:

- If standard diffraction experiments are not an adequate tool to experimentally extract structural information about this system, what other probes can we use that give information on the length scale of interest?
- How can we conciliate the structural picture extracted with local probes with the one provided by standard diffraction experiments? In other words, what types of distributions of heterogeneous domains can give rise to structures that are compatible with both the long-range average structure reflected in diffraction patterns and local structure?
- How does the existence of the chemically ordered $L1_0$ phase express itself, if at all, on the electronic and measured magnetic properties of the system?
- How can we explain the formation and stability of embedded nanoscale domains from the perspective of energetic/entropic arguments? This is probably one of the hardest issues to understand for the present problem. It is easy to see that analytical models for this problem are necessarily complicated to devise and solve. On the other hand, simulations are also difficult to implement; because of the length scales involved, the number of unit cells/atoms required to obtain representative results is outside current computational capabilities. In this context, however, it is worth mentioning a recent work[13] in which a Ginzburg−Landau model for the coupling of strains to charge and magnetization degrees of freedom is simulated. By introducing the apparently innocuous constraint that the local stress produced by charge doping does not generate defects when deforming surrounding cells, anisotropic long-range elastic forces appear in the system that lead to the formation of multiscale texture that includes nanoscale phase separation, mesoscale inhomogeneities, and so forth.
- What tools can we use to calculate physical properties of such a system? For example, to calculate electronic properties, standard electronic structure methods based on supercell calculations are not applicable, as the disorder cannot be simply described as some isolated defects.

In the present work, we address these issues, dividing the results between two papers. In this first one, we will address the first two questions. XAFS measurements on 27-nm NiMn films near the equiatomic composition as a function of deposition temperature will elucidate the formation of the $L1_0$ phase and its relation to the remnant coercivity. A heterogeneous model of the structure that includes local $L1_0$ ordering on the nanoscale embedded in a chemically disordered fcc (or a variant of this one) is the best calculable interpretation of the XAFS data within the context of the two-phase model derived from crystallography. We also describe simulations of the structure factor and pair distribution functions for lattices composed of two nanophases. These will demonstrate the limits of the typical size and distribution (ordered vs disordered) of the minority phase so that it produces no noticeable signatures in diffraction patterns whereas it is easily identified with local probes. This is an essential component in the reconstruction of the arrangement of atoms because there is no method for extrapolating one-dimensional local structure data to longer length scales. It also provides a means for elucidating the effects of elastic strain on the nanoscale. In the second paper, we will present electronic structure calculations for $L1_0$ clusters embedded in an fcc matrix, reporting the local density of states and magnetization. These calculations will illustrate how current-day real space methods can deal with heterogeneous systems.

Introduction

NiMn in its chemically ordered state is a strong antiferromagnet (AF) and thus a good candidate for use as an exchange coupling material. It has been shown that the exchange bias decreases with decreasing AF layer thickness and that a critical thickness is needed to develop the exchange coupling. It has been suggested[14] that such thin films ($\leq 5-10$ nm) are not chemically ordered and hence are not AF, which explains the small exchange coupling in these films. In grazing incidence X-ray diffraction measurements up to $Q \sim 5$ Å^{-1} on NiMn films annealed at 280 °C over this range of thicknesses, no traces of sites in the $L1_0$ phase were found.[14] In 15−25 nm thick films, the chemically ordered $L1_0$ phase grows at the expense of the fcc phase, increasing the exchange bias to 300−400 Oe.

We start by exploring in detail the early stages of macroscopic $L1_0$ phase formation and the correlation between local order (below the diffraction limit) and the remnant coercivity in materials that exhibit only partial or negligible longer range (crystallographic) $L1_0$ ordering. In these samples, the ordering in a 27-nm-thick NiMn pinning layer was varied by the use of different substrate growth temperatures during the fabrication over a range from 3 to 200 °C. XAFS studies provide complementary information not only to diffraction data that gives the long-range average order but also to that obtained from diffuse scattering and pair distribution function analysis, which would be another means for probing the appearance and development of the nucleation sites for the $L1_0$ phase.[15,16] However, for thin, multilayer, heterogeneous films, the counting

TABLE 1: Growth Temperature, Exchange Bias Field, and Long-Range/Short-Range Order Parameters

sample	growth temp (°C)	Hex (Oe)	S_{LRO}	S_{SRO} ($R \sim 2.6$ Å)	S_{SRO} ($R \sim 4.9$ Å); fcc + L10	S_{SRO} ($R \sim 4.9$ Å); homogeneous
3C	3	29	<0.1	0.22 ± 0.17	0.32 ± 0.2	0.41 ± 0.2
30C	30	39.7	N/A	0.41 ± 0.22	0.47 ± 0.2	0.61 ± 0.2
100C	100	65	N/A	0.68 ± 0.23	0.52 ± 0.2	0.60 ± 0.2
200C	200	119	0.45 ± 0.06	0.85 ± 0.25	0.70 ± 0.2	0.70 ± 0.2

statistics, preferred orientation, intrinsic delocalization of the diffuse intensity in the diffraction pattern, and substitutional nature of the material make the analysis of the diffuse scattering intensity less than totally unique and unambiguous so that similar data from an independent measurement is of value.

In this work, we employed X-ray absorption fine-structure (XAFS) spectroscopy at the Mn *K*-edge as a direct and element specific probe of the average local atomic structure within ~5−6 Å of the Mn site. The primary issue, the separation and ordering of the fcc and tetragonal $L1_0$ phases, is not amenable to standard curve-fitting analysis because of the overlap of their structural parameters exacerbated by strain at the domain interfaces. Therefore, a somewhat unconventional approach was used. Instead of the usual metrical parameters, the XAFS spectra were used to determine a short-range order parameter, S_{SRO}, for direct comparison with the coercivity and the long-range order parameter, S_{LRO}, derived from the conventional X-ray diffraction analysis (to $Q \sim 4-5$ Å^{-1}) for our most and least ordered samples. The extent of the chemical order and associated tetragonal distortion in both diffraction and XAFS measurements is quantified following Warren's definition[15] valid for any arbitrary sized domain: S_{SRO} is zero for no chemical order and a symmetric local structure, unity for complete order and a tetragonally distorted environment, and is proportional to the number of Mn atoms residing on their $L1_0$ crystallographic lattice sites and the extent of the local distortion. An enhancement to this definition of S_{SRO} that is essential in this context of magnetic ordering within small domains of chemically and structurally ordered atoms is the incorporation into the determination of the order parameter of the possibility of cooperative behavior that would lead to discontinuities in the extent of local ordering. Such collective interactions between atoms would promote the formation of relatively highly ordered, nanoscale domains that could be embedded in a highly disordered host lattice and complicate the standard, crystallographic S_{SRO} by rendering it heterogeneous.

As is also true for extractions of order parameters from scattering data, the determination of S_{SRO} from the XAFS can only be performed within the context of a model that assumes specific end point structures. To perform this analysis, we have used the accepted crystallographic model described above that assigns the chemically ordered $L1_0$ structure to the ordered phase and the chemically disordered fcc compound and any other structures (e.g., strained $L1_0-L1_0$ or −fcc interfaces) to the disordered phase. The specific issue addressed by this work is therefore whether XAFS provides any indication that this structural/chemical (and magnetic) ordering process and its correlation with the exchange bias of the NiMn/permalloy films continues when the length scale of such ordering decreases below the diffraction limit. Although the analysis shows that the experimental data are consistent with this model, it is not feasible to demonstrate that it provides a unique solution. We will therefore be assuming this accepted model for the NiMn alloy rather than attempting to ascertain the validity of the model itself, which has not been an issue.

On this basis, we will show that even in disordered samples, such as a film grown at 3 °C where S_{LRO} is not distinguishable from zero despite nonzero exchange bias, the S_{SRO} is substantially larger than zero, indicating that formation of nondiffracting domains of the $L1_0$ phase that exhibit magnetic ordering can occur before the signature of this phase appears in the diffraction patterns. There is therefore a strong correlation not only between long-range but also local chemical order and exchange coupling, implying that $L1_0$ domains produce antiferromagnetism even when quite small.

Materials and Methods

$Ni_{1-x}Mn_x$ ($x = 0.52$)/permalloy ($Ni_{1-x}Fe_x$ $x = 0.2$) exchange-coupled bilayer films were grown in a V80H (VG Semicon Ltd.) molecular beam epitaxy machine under ultrahigh vacuum conditions with the pressure maintained below 2×10^{-10} mB during growth. Ni and Fe beams were generated from e-gun evaporation sources and Mn from an effusion cell. NiMn and permalloy growth rates were ~0.1 and 0.2 Å/s, respectively. The films were grown on Spectrosil (SiO_2) wafers prepared by immersion in a solution of 1:1:100 $NH_4OH:H_2O_2:H_2O$, followed by a rinse in H_2O and dried in a jet of N_2 gas. Permalloy films of ~100 Å thickness were grown first with the substrate temperature 30 °C followed by NiMn, ~270 Å thick, grown with the substrate at 3, 30, 100, or 200 °C (samples 3C, 30C, 100C, and 200C, respectively). A capping layer of ~40 Å Pd was deposited at a substrate temperature of ~20 °C. The samples were grown with a magnetic field of ~1000 Oe in the film plane, during growth, to produce a uniaxial magnetic anisotropy in the permalloy. Following growth, the films were characterized by the longitudinal magnetooptical Kerr effect. The exchange bias values given in Table 1 are modest compared to the ~300 Oe expected for such structures when annealed at ca. 260 °C.[14]

X-ray diffraction spectra of samples 3C and 200C were taken at beamline ×20A of the National Synchrotron Light Source at room temperature. The data were collected using grazing incidence geometry that predominantly measures planes parallel to the film surface. The long-range order parameter was quantified from the intensities of the (110) and (220) peaks as described in ref 13 and is listed in Table 1.

Mn *K*-edge XAFS spectra were measured at beamline 4-1 of the Stanford Synchrotron Radiation Laboratory (SSRL) using a Si (220) double-crystal monochromator. Harmonic rejection was accomplished with a Rh-coated mirror aligned to provide a cutoff energy of ~9 keV. The data were taken in fluorescence yield mode using a 13-element Ge detector with energy resolution ~260 eV to collect the partial K_α yield at the Mn *K*-edge. Two or three scans were collected from each sample to ensure data reproducibility and to improve the data quality by averaging. All films were attached to the coldfinger of a liquid-nitrogen cryostat with maintaining the temperature at ca. 80 K. The samples were oriented to provide essentially bulk sensitive measurements: the incident X-ray and central detector acceptance angle were both ~45° to the surface of the film. Since the films are less than 300 Å thick, the XAFS spectra were not corrected for self-absorption. XAFS data were reduced following standard procedures.[17] The $\chi(k)$ spectra weighted by

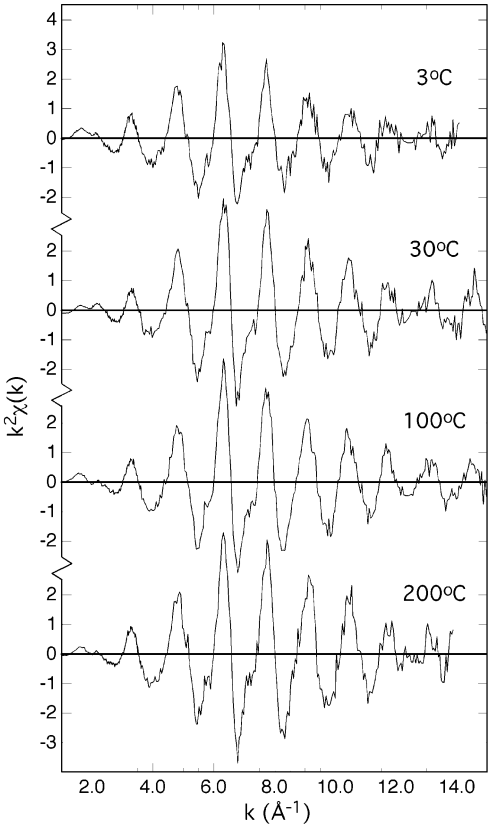

Figure 1. Mn *K*-edge $k^2\chi(k)$ vs k for indicated samples.

k^2 are shown in Figure 1, demonstrating good data quality up to 13−14 Å^{-1} ($Q = 2k \sim 26$ Å^{-1}). The details of the further analysis and extraction of the S_{SRO} will be described in the next section.

Results

Magnitudes and real parts of the Fourier transform (FT), the $\chi(R, k^2)$ representation, of the spectra of all four films are shown in Figure 2. The first peak ($R \sim 1.4-2.8$ Å) is due to single scattering of photoelectrons by the nearest-neighbor shell whose composition may vary from an average of six Mn and six Ni atoms at ∼2.60 Å in the chemically disordered fcc phase to eight Ni at ∼2.56 Å and four Mn atoms at ∼2.63 Å in the chemically ordered, tetragonally distorted $L1_0$ phase. As could be expected from the greater degree of crystallinity and long-range order induced by higher substrate temperature and consistent with the amplitudes of the $k^2\chi(k)$ data from Figure 1, the amplitude of this peak increases with increasing deposition temperature. The very small difference between 30C and 100C may result from the competing effect observed in the simulated spectra in the same figure; the tetragonal splitting foments static disorder that reduces the amplitude of this peak. These two opposing factors affecting the order, chemical ordering, and tetragonal splitting may therefore have crossed between substrate temperatures of 30° and 100 °C, giving the pattern observed in the spectra. The group of peaks in the range $R = 2.8-5.5$ Å is due to the combined contributions from the second through fifth shells and various multiple scattering contributions. It is in this extended region that the different arrangements of atoms in the two structures begin to produce separate spectral signatures and not just amplitude reduction as the separations between the positions of the shells increase beyond the resolution limit. Relative to that of the fcc structure, the calculations show that the spectrum of the $L1_0$ phase is notable for the convergence

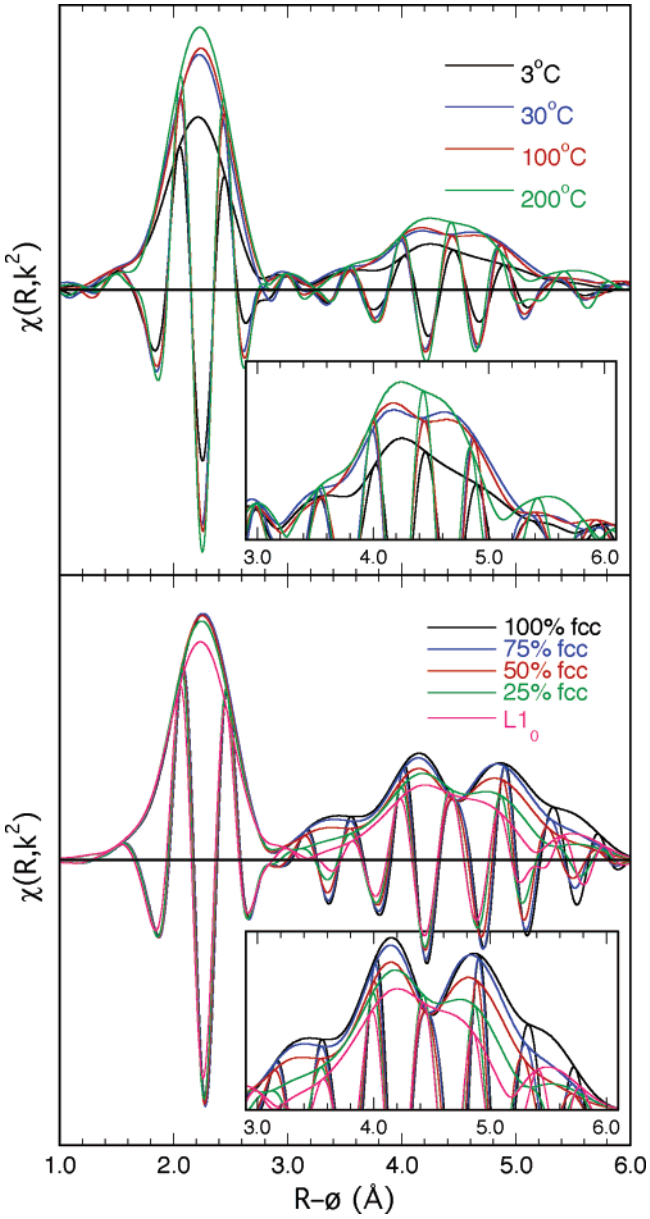

Figure 2. (upper) Fourier transform magnitude and real component of $k^2\chi(k)$ for indicated samples: 3C (black), 30C (blue), 100C (red), and 200C (green). The FT range is $k = 2.8-13.6$ Å^{-1}, and a sine window function was applied. (lower) Fourier transform magnitude and real component of calculated $k^2\chi(k)$ for indicated structures. The transform range and window is the same as used for the experimental spectra. The insets magnify the extended region containing the contributions from the second to fifth shells.

of the two principal peaks near $R = 4.1$ and 4.8 Å and the concomitant splitting off of the peak near 5.4 Å. A similar effect is easily observed in the spectra from 30C, 100C, and 200C, indicative of increased $L1_0$ ordering. However, the importance of general disorder is again prominent insofar as the 3C spectrum, while displaying a relatively large feature at $R = 3.5$ Å and an unresolved feature at 5.0 Å that proceeds smoothly to the small feature at 5.4 Å that are all characteristic of the fcc spectrum, is significantly lower in amplitude than the 200C spectrum despite the opposite behavior in the calculations. Although the fcc structure constitutes the long-range average as well as provides a large fraction of locally ordered atoms in this sample, there is apparently additional local disorder involving a significant fraction of the atoms that results in overall amplitude reduction of the EXAFS.

A. Derivation of S_{SRO} from Curve-Fits of the Nearest-Neighbor Shell Contribution. Because of the observed trends in the spectra, the prior knowledge of this system that provides a model for interpretation, and the ability to isolate the well-separated first-shell contribution to the EXAFS, one means for obtaining S_{SRO} is curve-fits of the first-shell contribution to the spectra. This was accomplished by performing two sets of constrained fits to the first-shell component of $\chi(k)$ that used either one or two Gaussian shells and by comparing the fit quality and other parameters. Model "1S" uses a single Mn−{Ni, Mn} average distance with the number of nearest neighbors fixed to 12. Model "2S" uses two different Mn−{Ni, Mn} distances and tests the possibility that the system is better described as two discrete structures, as discussed below. For the 3−11.8 Å^{-1} range of these fits in k-space and 1.4−2.8 Å in R-space, the number of free structural parameters (degrees of freedom) available in a curve-fit is seven,[18] which is the number used in the 2S fit, precluding more elaborate models. We shall further assume that (i) the Mn−{Ni, Mn} pair distribution functions (PDFs) are satisfactorily described using the Gaussian approximation and that (ii) the typical size of the domains exceeds 5−6 Å (cutoff limit of XAFS). The former assumption enables a conventional XAFS analysis procedure with a single parameter describing the shape of the distribution, while the latter allows the use of the FEFF code[19] to calculate the amplitudes and phase shifts including those modified by multiple scattering effects. The validity of the approximations made will be discussed in section IV. Since the Mn and Ni atoms are close in atomic number (Z_{Mn}= 25 vs Z_{Ni} = 28), the sensitivity of the XAFS analysis to their chemical identity is diminished. This justifies the use of Z = 26 Fe as an effective backscattering average atom in the first approximation as a means of simplifying and reducing the number of parameters in the fits by fitting both types of atoms with a single amplitude/phase combination. In addition, although the separation of the shells in the 2S fit is under the resolution limit of the spectra, the addition of a second, albeit unresolved, shell whose amplitude (corresponding to its number of atoms) is allowed to vary in the fit nevertheless modifies the distribution from harmonic and carries over into the details of the amplitude and phase. These alterations allow the quality of the fit to be used as a figure of merit in examining the two models.

Model 1S provides a poor fit for all films. For the least ordered film 3C (presumably containing the largest fraction of chemically disordered fcc and related structures), the best fit (dots) is compared to the Fourier filtered contribution to the $k^2\chi(k)$ (solid line) in Figure 3. Not only are there substantial deviations from the amplitude, but there are also ostensibly small ones in the phase that are actually very significant because of the high degree of accuracy to which the phase can be determined and its relative sensitivity to different types of disorder. Much better results are achieved for model 2S. Initially, the refinements were performed allowing the interatomic distances, Debye−Waller (DW) factors, and the energy shifts (ΔE_0) of both shells to be varied. The occupation numbers were constrained, so that $N_1 + N_2 = 12$. The parameters extracted for all samples indicate that both energy shifts and DW factor for bond length R_2 are $\Delta E_1 = 9.5 \pm 0.5$ eV, $\Delta E_2 = 4 \pm 0.3$ eV, and $\sigma^{(2)} = 0.022 \pm 0.001$ Å^2, respectively. Therefore, these parameters were fixed to further improve fit reliability. Forcing the two ΔE values to be equal gives almost identical results with almost negligible degradation in the quality of the fits, indicating that within this shallow curve in the fitting space this 5.5 eV difference simply compensates for, for example, anharmonicity in the distribution that gives an effective total $N <$ 12, forcing low k interference to reduce the amplitude or difference in the low-energy portion of the Fe phase shift relative to those of the Ni and Mn that are actually there. A reduced agreement factor for the constrained 2S fit, which accounts for degrees of freedom in the fits, was ∼1.5−1.8 times smaller than those obtained for the 1S model, depending on the sample. The constrained model 2S for sample 3C, shown by a dashed line in Figure 3, nicely reproduces the experimental data over the whole range of the plot, in contrast to the poor fit using the 1S model.

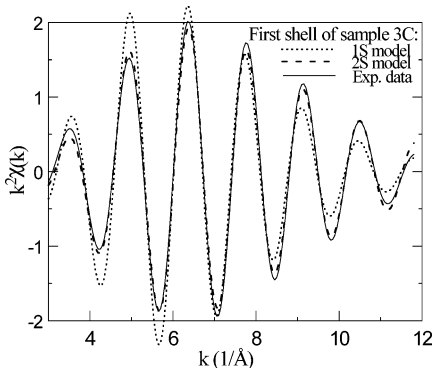

Figure 3. Comparison of the Fourier filtered data (solid line) from the first shell (principal peak from Figure 2) with curve-fits using models 1S (dots) and 2S (dashed line). The model 2S provides a much better fit over the whole range of the plot. Structural parameters extracted from the nonlinear least-squares fit 2S are summarized in Table 2.

TABLE 2: Local Structural Parameters Derived from the 2S Fit to Fourier Filtered Contribution of the First Peak[a]

	constrained two-shell (2S) fit			
sample	R_1, Å	N_1	$\sigma_1^{(2)}$, Å^2	R_2, Å
3C	2.578 ± 0.01	6.4 ± 0.4	0.0069 ± 0.001	2.619 ± 0.01
30C	2.576 ± 0.01	6.9 ± 0.5	0.0063 ± 0.0008	2.625 ± 0.01
100C	2.581 ± 0.01	7.4 ± 0.6	0.0057 ± 0.0009	2.63 ± 0.01
200C	2.578 ± 0.01	7.7 ± 0.6	0.0061 ± 0.001	2.632 ± 0.01

[a] The amplitudes and phase shifts were generated by FEFF-6 code[16] assuming the cubic fcc with a = 3.66 Å. Further details of the fit: $S_0^2 = 0.96$. For the ranges of the fit in k-space of 3−11.8 Å^{-1} and 1.44−2.76 Å in r-space, the allowed number of fitting parameters is 7. The total number of the parameters used in the fit is 4. Constraints were used: N_2 = 12-N_1, ΔE_1 = 9.5 EV, ΔE_2 = 4 EV, and $\sigma_2^{(2)}$ = 0.022 Å^2. Overall quality of the fit is illustrated in Figure 3.

To test for the chemical ordering associated with the tetragonal distortion, the effective backscattering amplitudes and phase shifts were replaced by the amplitudes and phase shifts for Mn−Ni (for the longer distance) and Mn−Mn (for the shorter distance) pairs, and the 2S fit was attempted again for the most ordered sample, 200C. The quality of the fit improved, but by a statistically insignificant amount. This indicates that, as expected, the EXAFS analysis did not distinguish between Ni and Mn atoms in the first shell and validates the simplification of the fits by modeling both the Mn−Ni and Mn contributions with composite Mn−Fe amplitudes and phases. Our EXAFS data for each substrate temperature are therefore not directly sensitive to the chemical order. Nevertheless, the substrate deposition temperature behavior of the 2S structural parameters summarized in Table 2 is consistent with growth of the chemically ordered $L1_0$ phase at the expense of the chemically disordered fcc one as this temperature is increased. This is a continuation of the same trend found in diffraction measurements, now extended below the point where signatures

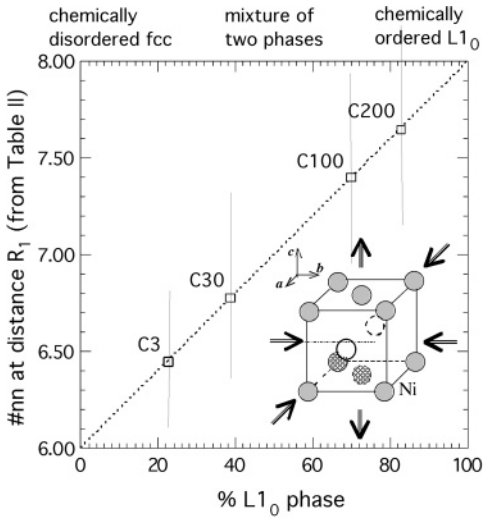

Figure 4. An estimate of the amount of $L1_0$ phase in the chemically disordered FCC matrix in the 2S model described in the text. The insert shows the chemically ordered $L1_0$/fcc phases.

of the $L1_0$ structure are discerned. Indeed, as one can see from Table 2, as the temperature increases from 3 to 200 °C, the number of atoms in the shell at $R_1 \sim 2.58$ Å steadily increases in magnitude at the expense of the occupancy of the longer distance contribution and also becomes narrower. It is, therefore, natural to associate this shell with a group of Mn−{Ni, Mn} distances mostly belonging to a phase whose domains are increasing in number and size, while the broader shell at $R_2 \sim 2.63$ Å is the contribution of other types of structures whose fraction is decreasing.

A feasible microscopic model for a $Ni_{1-x}Mn_x$ ($x \sim 0.52$) film prepared as described in the preceding section could therefore be a mixture of end member domains (chemically ordered tetragonal $L1_0$ and chemically disordered fcc) and low-symmetry, chemically disordered, and structurally strained aperiodic intermediate domains interfacing between the two phases and between $L1_0$ domains that are incoherent because they are out of registry with each other. This three-phase system can be reduced to the two-phase model 2S if we introduce *effective* fcc and *effective* $L1_0$ phases consisting of the fully ordered structures expected in the cores of the two domains in combination with the atom pairs from the strained interfacial regions that most resemble these structures. This model assumes within the fitting process that a continuum of distances would naturally be modeled by a combination of two end point structures and that this description both fits the spectra and gives an accurate representation of the relative amounts of the two structures. We then divide the nearest-neighbor distances Mn−-{Ni, Mn} into one that corresponds to the shorter distance of tetragonal $L1_0$ and a second containing all other distances of the effective fcc and $L1_0$ averaged together. The chemically disordered fcc phase is characterized by six Ni and six Mn atoms in the first shell. For the chemically ordered tetragonal $L1_0$, the number of Mn−Ni pairs increases to eight at the expense of Mn−Mn pairs. If a mixture of the chemically disordered fcc and the ordered $L1_0$ phases is considered, the number of Mn−Ni pairs is given by a calibration curve shown by the dotted line in Figure 4. Within the uncertainty of the 2S model, all of the extracted occupation numbers corresponding to the shortest bond length ($R_1 \sim 2.58$ Å) fall on the calibration curve, providing an estimate for the amount of the chemically ordered $L1_0$ phases in 3C, 30C, 100C, and 200C samples as $\sim 0.22 \pm 0.17$, $\sim 0.41 \pm 0.22$, $\sim 0.68 \pm 0.23$, and $\sim 0.85 \pm 0.25$. This estimate implies that the narrow peak at $R_1 \sim 2.58$ Å represents the short Mn−Ni bonds in the chemically ordered $L1_0$ phase. It disregards the overlap between the narrow and the broader peaks that are only 0.05 Å apart. The overlapped area, perhaps, should not be counted toward the amount of the $L1_0$ phase. However, large error bars for coordination numbers corresponding to the bond length R_1 obtained from the EXAFS fit (see Figure 4) makes this and several smaller possible corrections untenable. Therefore, Figure 4 represents the weight of the $L1_0$ phase in the chemically disordered fcc matrix that coincides with the definition for the local order parameter at a typical probe length scale of ~2.6 Å.

It needs also be asked whether the two distances found by the 2S model, which are determined with a much greater precision than the numbers, are self-consistent. These two distances are in fact in reasonable agreement with those estimated from both commonly used descriptions for alloys: (i) The continuum or homogeneous model based on diffraction results that assumes that the Mn−{Ni, Mn} distance at the peak of a single-site distribution curve scales linearly with the amount of the $L1_0$ phase in the fcc matrix to give $R_1(x) = 2.6065 - 0.0419x$ and $R_2(x) = 2.6065 + 0.0252x$ (Å) and (ii) the discrete or heterogeneous model in which the local fcc and $L1_0$ domains retain the Mn−{Ni, Mn} distances of the end members in a multisite distribution so that the 8 shortest Mn−Fe bond lengths of $L1_0$ are $R_1(x) = CONST = 2.5646$ Å and the 4 long bond lengths of $L1_0$ (2.6317 Å) and the 12 bond lengths of FCC (2.6065 Å) group together to yield the averaged $R_2(x) = (31.278 - 20.7512x)/(12 - 8x)$ (Å). Over the range of x determined from the numbers of atoms calculated by the curve-fits, 0.22−0.85, R_1 and R_2 go, respectively, from 2.597 to 2.571 and 2.612 to 2.628 Å in the continuum approach and are constant at 2.565 and increase from 2.609 to 2.623 Å with the discrete approach. These can be compared with the 2S results, in which R_1 is essentially constant at 2.578 Å and R_2 increases from 2.619 to 2.632 Å. The experimental distances are therefore all within <0.02 Å of the calculations, and the 0.04 Å separation between R_1 and R_2 is also very close to the models. The distances as well as the numbers of atoms are therefore in complete agreement with the assumption that the amount of effective $L1_0$ phase increases and effective fcc phase decreases with increasing deposition temperature. Although the quality of the data is insufficient to definitively indicate whether the continuum or discrete approach fit the data better, the constant R_1 and moderately increasing R_2 are more consistent with the latter. More information on this as well as corroboration of the S_{SRO} pattern are found in the contributions of the more distant neighbor shells.

B. Derivation of S_{SRO} from the Contribution of More Distant Shells. Beyond the first shell, the EXAFS is more complicated because the material is composed of a mixture of fcc- and $L1_0$-like structures and disordered interfacial regions between the two. The extended EXAFS over the region containing the contribution of the third to fifth shells was therefore analyzed by first isolating it by backtransforming the $\chi(R, k^2)$ spectra from $R = 3.2-5.9$ Å (Figure 2) and then fitting the backtransformed data with combinations of calculated composite structures on the basis of the two different ordering models instead of with individual shells. This process has also been termed "group" fitting. The heterogeneous model (corresponding to model "ii" in the first-shell analysis) was tested by fitting the backtransformed data with the calculated $\chi(k)$'s of the 100% ordered fcc and $L1_0$ structures backtransformed over the same region, varying only their relative amplitudes and σ's.

TABLE 3: Group-Fitting Results for Third to Fifth Shell Region

sample	3C		30C		100C		200C	
model	hetero[a]	50[b]	hetero	50[k]	hetero	75[c]	hetero	75
error[d]	0.102	0.094	0.096	0.056	0.119	0.116	0.147	0.149
N fcc[e]	0.296	0.144	0.217		0.123	0.283	0.080	0.244
σ fcc[f]	0.082	0.086	0.051		0	0.055	0	0
N $L1_0$[g]	0.322	0.606	0.467	0.821	0.524	0.390	0.700	0.520
σ $L1_0$	0.052	0.059	0.020	0.056	0.032	0	0	0.020
% $L1_0$[h]	32	41	47	61	52	60	70	70
% fcc[i]	30	34	21	21	13	7	8	6
% amorphous[j]	38	25	32	18	35	33	22	24

[a] Hetero = heterogeneous structure model; fit with fcc + $L1_0$ EXAFS. [b] 50 = homogeneous/continuous structure model; fit with 50:50 + 25:75 fcc:$L1_0$ ordered structure EXAFS. [c] 75 = homogeneous/continuous structure model; fit with 25:75 fcc/$L1_0$ ordered structure + $L1_0$ EXAFS. [d] Least-squares error. [e] fcc or 50/75% $L1_0$-ordered amplitude factor from fit based on amplitude from FEFF calculation = 1.00. [f] Debye−Waller factor for fcc or less ordered homogeneous component. [g] $L1_0$ or 75/100% $L1_0$-ordered amplitude factor from fit based on amplitude from FEFF calculation = 1.00. [h] % $L1_0$ ordering, $L1_0$ amplitude factor for heterogeneous fits, extrapolated $L1_0$ ordering normalized by the sum of the amplitude factors of the two components for homogeneous structure fits. [i] % fcc ordering, same as footnote *h*. [j] % amorphous component = 1.00 − the sum of the amplitude factors from the two ordered components. [k] The optimum 30C homogeneous structure model fit utilized only the 75% $L1_0$ ordered spectrum.

For the homogeneous ordering mechanism, model "i", $\chi(k)$'s were created by backtransforming over the same region as the $\chi(R, k^2)$ calculated from the 25, 50, and 75% $L1_0$ continuously ordered structures defined as above (0 and 100% $L1_0$ are the end point structures). In calculating the spectra, the damping was initially set by using the same Debye temperature for the fcc and $L1_0$ structures that gave the best match to the amplitude of the experimental $\chi(R, k^2)$ spectrum for the first peak at R = 1.4−2.8 Å. The experimental data were then fit by the two composite spectra from structures that bracketed the nearest-neighbor results. In all cases, the total number of atoms in the calculated spectrum was set equal to 1.00 after backtransformation so that the N from the optimized fit corresponded to the fractional amplitude of the spectrum calculated from the assumed structure. S_{SRO} was then defined as the amplitude of the more highly $L1_0$ ordered spectrum used in the fit, multiplied by the fraction $L1_0$ for the heterogeneous, model i fits. The fraction fcc was obtained similarly, and the difference between the total amplitude and one was used as the fraction of disordered material that does not contribute to the EXAFS (Table 3). The results so obtained are strikingly similar to those from the analysis of the first shell. Since, as expected, the distances only varied from their original positions by at most an insignificant ±0.02 Å, and less when the amplitudes of the two structures were comparable, they are not included in the table.

The validity of the assumed model involving only a combination of fcc and $L1_0$ structures as contributors to the EXAFS is indicated by the quality of the fit (Figure 5). Since the crystallographic model has already been successful in explaining materials with long-range order and short-range order for the nearest-neighbor shell in the EXAFS for samples below the diffraction limit, it is not surprising that these fits are excellent. They are only slightly marred by some small deviations in the real component at high R and a somewhat flatter modulus in the fit relative to the data for the 3C and 200C spectra.

Because of the ambiguity in the fits between the hetero- and homogeneous models, these group fits were supplemented by comparing the measured with the calculated phase shifts from both types of ordering for the 0, 25, 50, 75, and 100% $L1_0$ ordered structures over this entire region in R. The phase can be highly sensitive to the details of the pair distribution. The phases from both the data and calculated spectra are obtained as part of the backtransform process and are then converted into phase shifts by subtracting $2kR_{ave}$ with $R_{ave} \sim 4.91$ Å representing the nominal average distance of the third and fourth

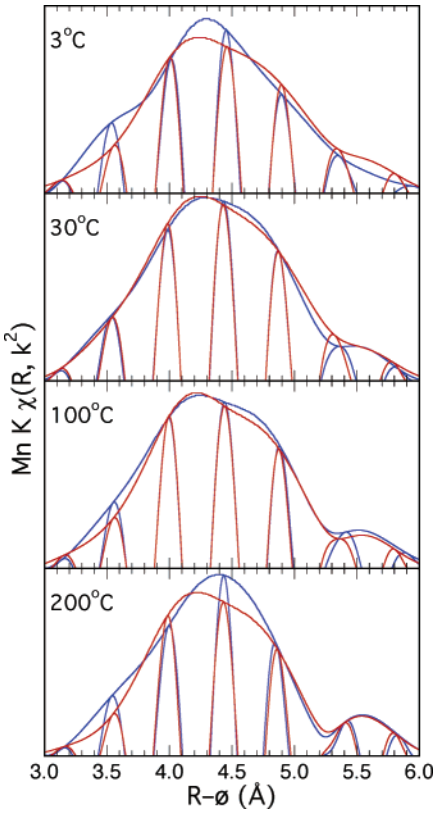

Figure 5. Data (blue) and group fits (red) in which the spectra over this range were fit by a combination of two full spectra calculated by FEFF from the continuum model for the transition.

shells. Prior to the advent of accurate and fast codes for calculating χ, such direct comparison of the isolated phase (albeit from single shells of neighbor atoms) with those from standard compounds was a highly developed approach used not only for extracting distance information but also for quantifying the degree of chemical similarity.[20]

Inspection of the calculated phase shifts shows that they potentially are a sensitive and accurate measure for both the $L1_0$ fraction and, serendipitously, the mechanism whereby it evolved with increasing substrate temperature. The phase shift around k = 9 Å^{-1}, which is mostly due to the destructive interference between the single scattering waves from the third and fourth nearest neighbors, moves to higher k in a regular way with increasing $L1_0$ content (Figure 6) with a concomitant

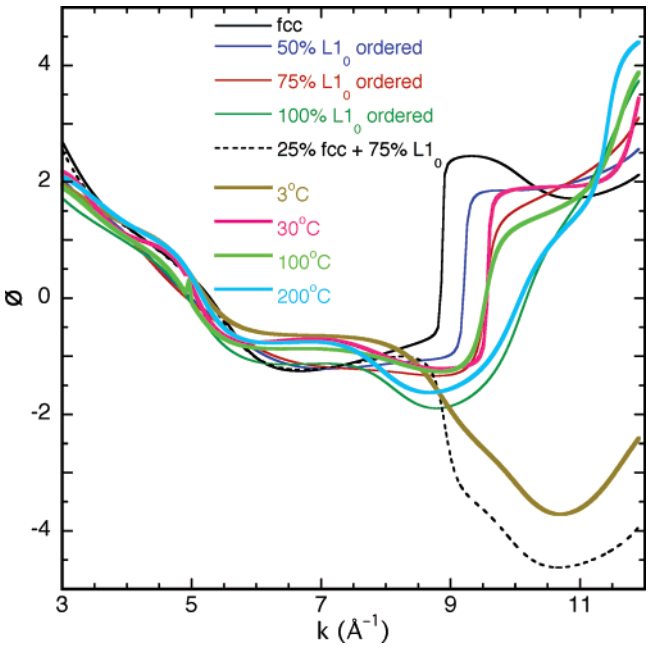

Figure 6. Reduced phase factors about the beat at ~9.5 Å^{-1} for indicated samples are compared to those calculated by FEFF from various chemical models described in the text. Back Fourier transform range is ~3.9−5.0 Å for all spectra.

decrease in slope and transfer of curvature from its upper to lower portion. On either side of the phase shift, increased $L1_0$ content is also reflected in other changes, a downward bend below it and an upward slope above it. In addition, the homogeneous/continuum and heterogeneous/discrete approaches are differentiated dramatically by the phase shift of the former going up and the latter going down. The impact of multiple scattering contributions on the observed phase shift behavior was evaluated by additional calculations in which the most pronounced contributions were reduced by tilting local domains by up to 10 degrees to misalign the first and the fourth neighbors. These simulations showed that, although the shape of the phase shift is slightly modified by these rotations, its position at ~9.5 Å^{-1} is unaffected and the overall effect of disorder on multiple scattering contributions on this application of the phase shift is minor. Within the context of the crystallographic model, the phase shift from this extended region of the local structure therefore is capable of providing a sensitive and accurate means for deriving S_{SRO} and for differentiating between the continuum and discrete models for the development of the homogeneous $L1_0$ end point structure.

The comparison of these calculated phase shifts with the experimental results (Figure 6) show remarkable agreement between the two. Not only are the phase shifts near $k = 9$ Å^{-1} observed at the same locations with the same amplitudes and directions, but also the overall shapes of the curves and their behaviors are surprisingly similar over the entire range. The experimental spectra exhibit the initial downward slope and subsequent flattening between $k = 5.5-8.0$ Å^{-1}, as well as emulating the continued flatness or downward bend, decrease in the slope of the shift itself, and continued rise that are all associated with greater $L1_0$ ordering when the phase shift proper is at higher energy. These observations further corroborate the crystallographic model below the diffraction limit. Insofar as the entire phase shift is quite sensitive to the relatively subtle nuances between the average structures of the discrete and continuum models, the fact that the experimental data emulate all of the features of the calculated shifts suggests that the given interpretation is unique without necessarily having to assume the crystallographic model.

On the basis of all of these attributes, but focusing on the phase shift region, it is strikingly apparent that increased annealing times are closely correlated with higher k values of the phase shift that are coupled to enhanced $L1_0$ ordering and S_{SRO}. In addition, the change in the direction of the phase shift from negative to positive between 3C and the other samples implies that the arrangement of atoms also is altered from the discrete to continuum type of structure. The combination of fcc and $L1_0$ domains at the lowest deposition temperature yields to an arrangement of atoms that gives an EXAFS spectrum more like that from a partly ordered, strained $L1_0$ environment at higher temperatures. This is consistent with (see below) the loss of the fcc fraction as a contributor to the EXAFS and small $L1_0$ domains that are strained throughout by epitaxial mismatch at their boundaries. In terms of extracting S_{SRO}, the shape and phase shift position for sample 3C are most consistent with 25% $L1_0/S_{SRO}$, 30C and 100C give 60−70% S_{SRO}, and for sample 200C the spectrum shows near complete short-range order, S_{SRO} ~ 100%. Estimated uncertainties in the short-range order parameter S_{SRO} ($R \sim 4.9$ Å) are ~0.2.

These results for S_{SRO}, although consistent, appear excessively high both in comparison with diffraction and the analysis of the first shell but also in that the reduced amplitudes demonstrate that the material cannot be fully ordered. The possible interpretations and applicability of this phase shift analysis were therefore further tested by considering a complex model PDF function that may mimic some of the behavior of the NiMn alloy (Figure 7). This distribution function, $g(r)$, consisted of two components: a single-ordered Gaussian shell and a quasi-rectangular, anharmonic, glasslike distribution centered at the same distance and containing the same total number of atoms at five equally spaced intervals that, when broadened by the same Gaussian, gives the $g(r)$ shown in Figure 7. A model $\chi(k)$ calculated from $g(r)$[21] was then fit with a single wave with the standard Gaussian Debye−Waller factor. Disconcertingly, simply by reducing the overall number of atoms by 29% and increasing the Debye−Waller factor from 0.090 to 0.105 Å, both results being physically reasonable values, an excellent curve-fit is obtained (Figure 7b) that gives only negligible indication of the broad, anharmonic part of the total $g(r)$. The quality of this fit is, in fact, so good, that the addition of a second shell to the fit was unable to improve it as the two shells converged into a single one. More accurate descriptions of the actual $g(r)$ required the use of at least three shells that had to start close to the correct values. The reason for this is apparent in the phase shifts plot in Figure 7c (total phase $- 2kR_{ave}$) of the calculated XAFS and its single-shell fit. These are almost identical, with the largest differences at the ends where the cutoff effects from the Fourier transform process distort the data anyway.

This result is significant in interpreting the phase shift analysis. The modeling demonstrates the ease of crafting a distribution that will reduce the overall amplitude but have only negligible effects on the phase, as is observed in the experimental versus computational results, Figure 2. The phase shift may therefore indicate a high degree of $L1_0$ order because it is sampling only the locally ordered fraction of the structure and is unaffected by atom pairs that compose a fraction with a broad, flat, "glassy" distribution of these more distant neighbors that is analogous to the model used in the calculation. Just as diffraction is insensitive to aperiodic structures, atoms whose local ordering is relatively even or flat over several tenths of an Å are invisible to EXAFS, resulting in a reduction in

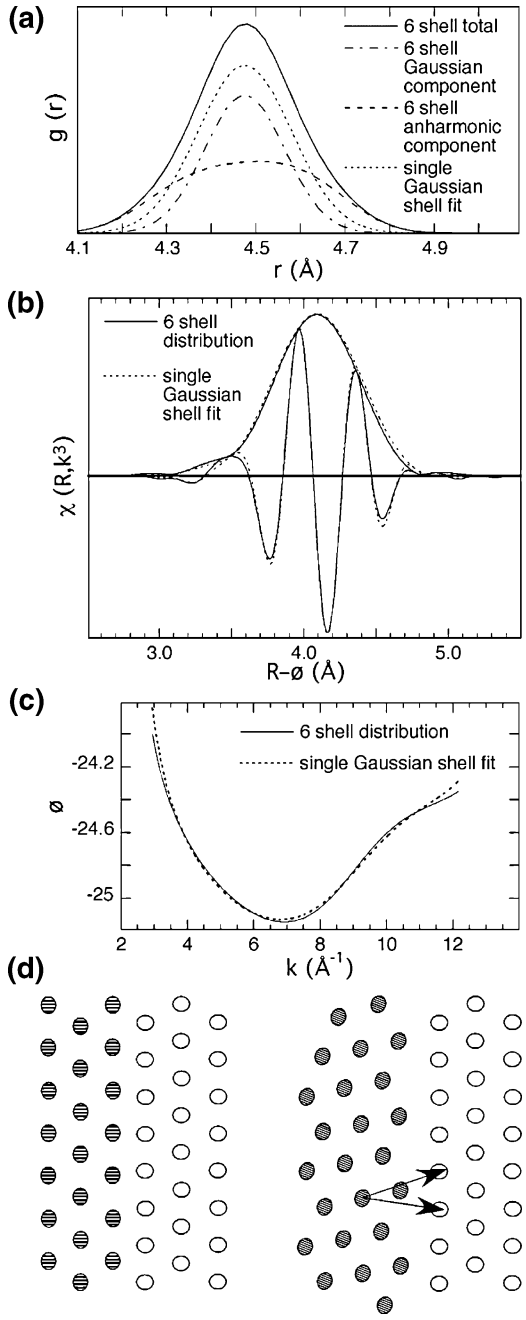

Figure 7. (a) An anharmonic distribution composed of six shells of atoms was created from the summation of a Gaussian component and a roughly rectangular distribution on the basis of an equal number of total atoms centered at the same distance consisting of five sets of atoms with the same Gaussian distribution spaced equidistantly. A single-shell Gaussian fit to the resulting EXAFS gave a reduced number of atoms with a larger width. (b) This single-shell curve-fit gives an excellent correspondence to the EXAFS of the anharmonic distribution, which exhibits negligible signature of the anharmonicity. (c) The phase shifts of the EXAFS of the six-shell anharmonic distribution and single-shell fit. (d) Interfacial strain between two orthogonal tetragonal domains can be partly relieved by rotating one of the domains and subsequently displacing it to restore the nearest-neighbor distances across the interface, which also results in symmetric splits of the second (and more distant) neighbor distances.

amplitude and an apparent reduction in the overall number of atoms. The phase shift is then also consistent with and suggests that the equilibrium ordered component of the local structure favors the $L1_0$ phase, so that domains with true fcc ordering are quickly lost and the actual arrangement of atoms becomes small, poorly coherent, locally ordered $L1_0$ domains separated by disordered (not fcc) interfacial regions. A more accurate S_{SRO} (at $R \sim 4.9$ Å) would therefore need to reduce the one obtained from the phase shift by a factor obtained from the extent to which the overall amplitude is diminished. If these glassy domains are averaged to the fcc structure over the longer diffraction length scale by conserving the average lattice even as the atoms are displaced from their lattice sites, then they could be the source of the fcc diffraction pattern even in the absence of atoms that are locally fcc. Reasonable arrangements of atoms that adhere to this rule can be devised. Incorporating the additional observation that any splittings within the first shell are small, we have shown previously that this modification to the distribution results from rotations and not displacements.[22] As an example, a well-matched interface for two initially orthogonal lattices with a 15% rectangular distortion results from a 22° rotation of one of the domains followed by a displacement to restore the original bond lengths across the interface, which also symmetrically splits the more distant shells. We do not intend to imply that this describes NiMn. It may well be that local rotations involving only a few or even individual sites at the interface rather than the entire domain will produce less total strain while maintaining orthogonality between the domain cores, and the actual interface structure is outside of the scope of this work. It does, however, demonstrate that the combination of small, incoherent, locally ordered $L1_0$ domains separated by interfaces that do not contribute to the EXAFS that is suggested by these results is feasible and physically realistic.

C. The Effects of Nanoscale Heterogeneity on *g*(*r*) and *S*(*Q*) in the Two-Dimensional Analogue of an fcc−$L1_0$ AB System. We now present results of a numerical model that explores possible mechanisms whereby the formation of nanoscale $L1_0$ domains prior to the observation of the $L1_0$ diffraction pattern can occur. We attempt to answer the following question: assuming that nanoscale structural separation or heterogeneity exists in the growth of $L1_0$ ordering, how and why is it detected with local probes (XAFS) before being explicitly observed in diffraction patterns in NiMn so that $S_{SRO} > S_{LRO}$? When correlations between local distortions produce ordered distributions, they are generally observed in diffraction experiments as superlattice or satellite peaks (in addition to the Bragg peaks).[25] The situation, however, is more complicated when domains below the limit of long-range order/diffraction limit in size that are distinguished by different structures occur in a random or aperiodic distributions,[26,27,28] which we have been referring to as nonclassical phase separation and nanoscale heterogeneity. In this case, the effects of heterogeneity, defect or other chemical organization, and competition between different phases on the diffraction patterns are not well understood. In a recent paper,[29] for example, we have shown that a second coexisting structure affecting one-fifth or more of the atoms in various two-dimensional lattices can have a minimal to negligible effect on the calculated structure factors when compared with their periodic counterparts. The signatures of disorder that are present in the diffuse part of the scattering are usually smooth and subtle, and it is often easy to construct several or even many distinct disordered lattices that produce essentially equivalent diffraction patterns. Here, using the example of the NiMn system, we investigate the effects that domain size and interface behavior have on conventional diffraction when nanoscale phase separation and heterogeneity occur below the diffraction limit.

To illustrate the disparity in the appearance of nanoscale heterogeneities between diffraction and local structure data

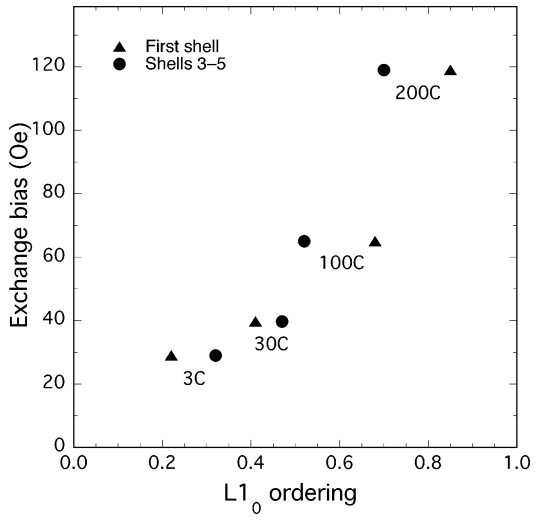

Figure 8. Correlations between exchange bias magnetic field measured by the longitudinal magnetooptic Kerr effect and local order parameter derived from our XAFS analysis for both the first-shell and extended structures.

(including EXAFS), we compare the geometrical structure factor

$$S(q) = \sum_{i,j} e^{i\mathbf{q}\cdot\mathbf{r}_{ij}}$$

and molecular pair distribution function

$$\rho(r) = \frac{1}{2\pi r}\sum_{i,j}\delta(r - r_{ij})$$

of various two-dimensional lattices. The lattices represent [111] planes of the NiMn alloy films discussed, within which the $L1_0$ structure is comprised of alternating rows of the two elements. Rectangular domains of various sizes of the $L1_0$ structure are embedded in a chemically disordered triangular matrix (hereafter referred to as fcc, as the disordered component gives this diffraction pattern in the bulk material), with each structure present in equal amounts. Atomic interactions described with a Rose potential[30] determine the precise atom positions required to minimize the total elastic energy. The equilibrium bond lengths are inferred from the observed fcc and tetragonal distances:[4] Ni−Ni = Mn−Mn = 2.63 Å and Ni−Mn = 2.56 Å, and a cutoff distance of 3.60 Å limits the interactions to nearest neighbors. The bond energies and moduli are equal for all three interactions, making the results independent of these values and thus simplifying the model significantly. The lattices are constructed with approximately one million atoms, and periodic boundary conditions are used in all calculations. Large lattice sizes are required to obtain the desired resolution in the diffraction data ($\Delta q \approx 0.002$ Å^{-1}), and as such three-dimensional simulations have exceeded our computational limits (although efforts are currently underway to overcome these limitations, and preliminary results indicate that our conclusions will remain the same). Finally, our results given here are averages obtained from 10 lattices. The ability to obtain a minimum elastic energy over such large lattices is a significant advance from our previous work, as we are able to demonstrate the importance of the elastic response of the lattice and the effects of defects.

The lattices are distinguished by the domain sizes of the $L1_0$ structure. A region of a typical lattice is shown in Figure 9. Portions of three domains show the possible orientations of the $L1_0$ chemical ordering as well as the chemically disordered fcc

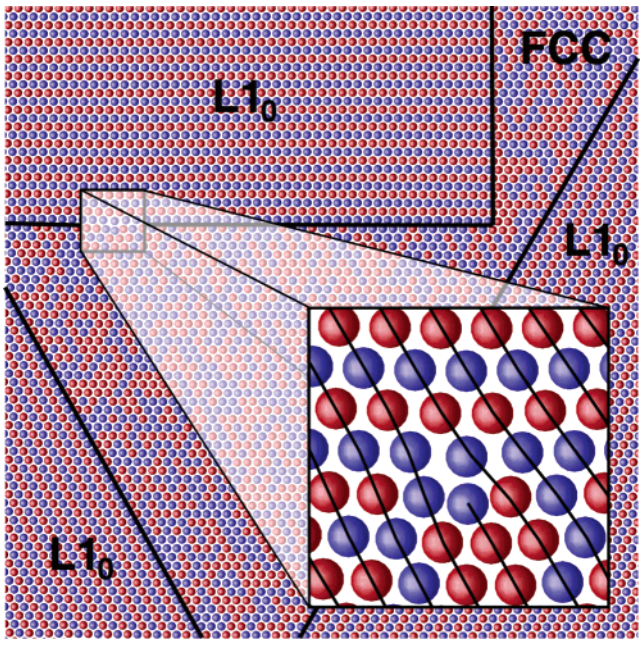

Figure 9. A [111] plane showing portions of three chemically ordered $L1_0$ domains separated by a chemically disordered fcc phase. The $L1_0$ structure in this plane has expanded atomic separations along rows of similar atoms and contracted separations between rows of different atoms, compared with the higher-symmetry triangular phase. For large domain sizes, this can lead to dislocations (inset) because of the mismatch between the two phases.

structure that separates them. Because the orientations of the domains are random, the material does not exhibit any gross anisotropic distortion so that changes in the average crystal length along both directions is equal.

The atoms within lattices with large domains are introduced in two ways to account for the subtle differences in the arrangement of interfacial atoms that might result from an annealing process. In one case, where neighbor exchange is the driving kinetic force, one might expect the domains and the matrix to remain coherent (i.e., each row of atoms extends across the entire crystal). This type of lattice is constructed by simply substituting each atom in a chemically disordered region with one appropriate for the creation of an $L1_0$ structure prior to minimizing the elastic energy. No dislocations occur in such a lattice, and the elastic energies can be quite high considering the various preferred bond lengths between the $L1_0$ and chemically disordered structures (a single crystal of the latter always gives a higher symmetry fcc structure with an average bond length of 2.60 Å).

The second type of lattice allows for dislocations at the interface of the two structures. These are constructed by replacing entire regions of the disordered structure with $L1_0$ domains containing the preferred atomic separations. For example, a rectangular domain with 80 rows and 80 columns of atoms of the disordered structure is replaced with an $L1_0$ domain with 79 rows and 81 columns, as those dimensions achieve a lower elastic energy than any others, even with the dislocations present (one is shown in the inset of Figure 9). The diffusion of atoms in an annealing process might account for the formation of these low-energy domains during crystal growth.

In Figure 10, we show the first five Bragg peaks in the diffraction data for lattices containing various $L1_0$ domain sizes (row × column). Even though all lattices are populated with 50 at-% of the $L1_0$ phase, the diffraction data for those with

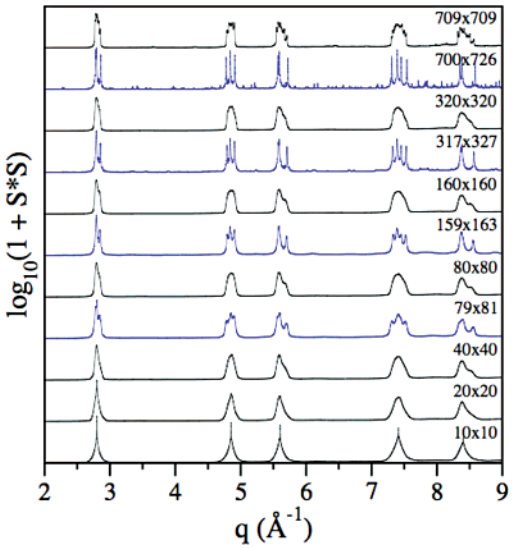

Figure 10. The intensity of the structure factor (log-scale) for lattices with various domain sizes. The presence of two structures only manifests itself in each Bragg peak in lattices that allow for dislocations (blue). Coherent structures without defects (black) either have significant interfacial stress that prohibits the formation of distinct structures or the domains are too small to resolve.

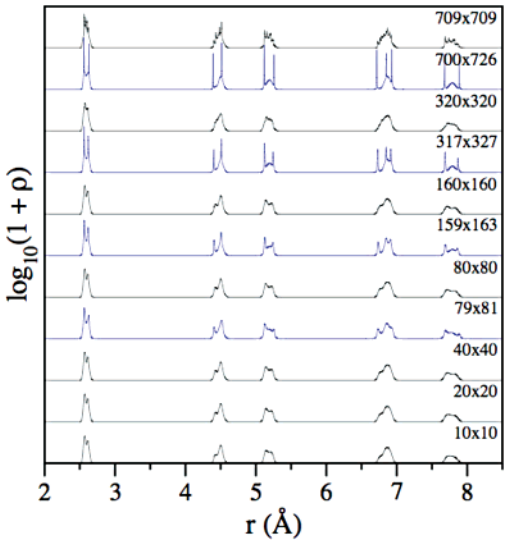

Figure 11. The molecular pair distribution function (log-scale) for lattices with various domain sizes. In all cases, it is possible to distinguish two structures in the system, thus providing insight into the local structure that diffraction data alone cannot.

smaller domains ($10 \times 10-40 \times 40$) give little indication of the presence of two coexisting structures. This is partly understood by considering that, at these sizes, the lattices are all coherent (giving the lowest elastic energy), and since the areas populated with the disordered structure have similar length scales to the $L1_0$ domains, much of the lattice can be described as purely interfacial regions. That is, the stresses involved between the two structures propagate throughout the lattices, and as a result the atom positions involve only small displacements from the perfect fcc structure that would be obtained by either averaging their positions or solving the diffraction pattern. In fact, with most peaks this trend continues for all coherent lattices (shown in black), independent of the domain sizes considered. The diffraction data from lattices with larger domains indeed have peaks that develop shoulders, but diffraction peaks never unambiguously show the presence of two separated phases, their relative amounts, and their exact crystal structure.

If lattices allow for dislocations (shown in blue), a significant relief in interfacial elastic energy is provided and atoms at the core of the $L1_0$ domains and disordered regions are able to relax to their desired structures. This is immediately apparent in the diffraction data, where even incoherent lattices with the smallest domain sizes have second, third, and fifth triangular peaks splitting to reveal structural details about the two phases. Only lattices with the largest domain size considered, however, are able to resolve the three length scales where the first triangular peak normally occurs.

In Figure 11, we show the molecular pair distribution for the same lattices. Interestingly, the distribution of lengths from the first through third nearest neighbors indicates the presence of two structures for even the smallest domain sizes (compare this with the diffraction data for domain sizes $10 \times 10-40 \times 40$). It is fair to say, then, that the diffraction data gives the long-range average order in the lattice, in the sense that small domains, each with ordered configurations but with various orientations and separated from each other by disordered interfacial regions, can indeed contribute diffraction signatures that globally average together to reveal only the high-symmetry triangular phase. In coherent lattices with small domains, the evidence corroborates the notion that local probes can detect small, nanoscale heterogeneities that are otherwise nonexistent in diffraction data. In the context of the NiMn alloy considered here, magnetic order is probably more correlated with the $L1_0$ chemical ordering than the tetragonal distortions. Also included in the figure are pair distribution functions of lattices that allow dislocations along domain interfaces (shown in blue), and like their associated diffraction data, they are able to resolve the two structures quite clearly.

Discussion

Comparing estimates of short-range order parameters with long-range order parameters available from X-ray diffraction analysis, S_{SRO} is always larger than S_{LRO}. The difference is clearly beyond the error bars of both experiments. A difference between S_{SRO} and S_{LRO} in a diffracting material is a sufficient condition for nanoscale phase separation and heterogeneity in the studied material because it demonstrates the presence of a nondiffracting but locally ordered component that must either be separate from the diffracting host or whose own domains must be separate from each other. This could also be described as nonclassical "phase separation" as the term is used in the correlated electronic oxides community, although in those materials the origin of the various mesoscopic textures is dynamical charge ordering and not static chemical ordering. Although the local ordering evolves into and eventually converges with the long-range ordering in the fully ordered limit, they need not be coupled during intermediate stages and a difference between them will reflect inhomogeneity or heterogeneity on length scales below the diffraction limit. The structure factor calculations suggest at least one mechanism whereby this difference between short- and long-range order are reconciled. This type of behavior is critical because the separate domains may retain the bulk properties pertaining to their individual structures so that the composite material may therefore continue to display such properties in apparent contradiction of the long-range order or may exhibit novel behaviors caused by the interactions between the domains.

NiMn films prepared at the lowest and highest growth temperatures are therefore heterogeneous on the atomic to

nanoscale length scales probed by this experiment. Since the most ordered samples are expected to form at the highest temperature, it is very likely that the two films grown at 30 and 100 °C are also heterogeneous. Why S_{SRO} is always larger than S_{LRO} can be explained: The typical size of domains that scatter elastically to give rise to the additional superstructure peaks in XRD is approximately the coherence length of the X-rays (typically tens to hundreds of angstroms). A large fraction of the 200C film consists of the smaller domains, which do not contribute to S_{LRO} because their coherence with each other is poor, that is, they are out of registry, or because this lack of coherence results in their average structure being fcc on the large diffraction length scale. However, these domains (which will be called nanodomains) do contribute to S_{SRO}, which is defined as the amount of the local $L1_0$ phase in the matrix that in turn displays an average (but apparently not local) fcc structure. Nanodomains exhibiting the $L1_0$ structure locally can occur long before the signature of the ordering appears in the diffraction measurements. S_{SRO} determination places limited constraints on the details of the tetragonal phase.[23] As a result, many distorted domains incorporating a large fraction of the material meet the EXAFS criteria for the local tetragonal distortions while they may fail to produce the crystallographic $L1_0$ phase, and vice versa for the fcc structure if it is locally disordered. The overall arrangement of atoms is therefore not so much inhomogeneous as heterogeneous on a nanometer scale, containing a large fraction of small, locally ordered, and aperiodic $L1_0$ domains within a host that averages to the fcc structure over the larger length scale of diffraction.

Considering the validity of the approximations made in the preceding section, S_{SRO} ($R \sim 2.6$ Å) $\approx S_{SRO}$ ($R \sim 4.9$ Å) suggesting that typical size of the ordered domains exceeds the EXAFS cutoff limit (~5−6 Å) in all dimensions. Beyond this, the length scales and coherence may not be isotropic, and we have recently demonstrated that long serpentine or filamentary domains may have only minimal signatures in diffraction.[12] A harmonic approximation for Mn−{Ni, Mn} PDFs requires small Gaussian disorder. If the local structure is distorted, these distortions are most apparent at higher *r*-values. Poor agreement between amplitudes of the experimental and the model EXAFS from the third to upper shells may be a signature of non-Gaussian character of the pair distribution functions for $R \geq 3-4$ Å, as shown in the calculation. The first-shell EXAFS analyses indicate that the shortest bond Mn−{Ni, Mn} (at $R_1 \sim 2.58$ Å) is reasonably harmonic, while the longest bond (at $R_2 \sim 2.63$ Å) shows traces of anharmonicity: $\sigma_2^{(2)}k^2 > 1$ for $k \geq 7$ Å^{-1}. Since the split between R_1 and R_2 is small and Mn−Ni pairs are not distinguishable from Mn−Mn pairs, the total PDF Mn−{Ni, Mn} is anharmonic, implying that the model 2S is one of the possible structural solutions and that there is no unique unfolding into effective $L1_0$ (about eight Ni atoms at ~2.56 Å and about four Mn atoms at ~2.63 Å) and effective disordered fcc (broad peak of about six Ni and six Mn atoms at ~2.58 Å). Nevertheless, EXAFS analysis indicates that the structure of $Ni_{1-x}Mn_x$ ($x \sim 0.52$) films grown at applied magnetic fields of 1 kOe and moderate substrate temperatures are more ordered than would be suggested by X-ray diffraction data, albeit on a smaller length scale. This conclusion on the heterogeneity in the NiMn films follows from consideration and reconciliation of both the XAFS and XRD results. It is important to realize that combined refinements of multiple data sets that begin with the crystal structure will not find such heterogeneous structures because there is no path to them in Monte Carlo simulations.

The heterogeneity of the NiMn films may evidently cause electronic and magnetic properties that are unexpected because they originate in local rather than bulk average characteristics of the lattice. This is precisely the purpose of the second paper of this series, where we will report results of real space electronic structure calculations for clusters containing $L1_0$ magnetic clusters embedded in a chemically disordered fcc matrix. This paper will show how the exchange bias field observed by the longitudinal magnetooptic Kerr effect can be attributed to the $L1_0$ nanodomains. Data in Table 1 indicate that the exchange bias increases with higher substrate deposition temperatures. Recalling that three types of microscopic domains form the film structure (fcc, $L1_0$, and interdomain/interfacial regions), we note that the amount and ordering of the observed $L1_0$ phase increases as this temperature is raised. If the interfaces were responsible for the observed behavior, one would expect to observe the exchange bias peaking with equal amounts of fcc and $L1_0$ phases, providing the largest interface volume. Therefore, by exclusion, the magnetic behavior is due to the $L1_0$ phase, which is consistent with the observed behavior of the bulk materials. Figure 8 shows the dependence of the exchange bias versus fraction of the $L1_0$ phase (S_{SRO} from both first-shell and extended analyses) assembled using data from Table 1. The bias increases faster than the volume fraction of the tetragonal phase, suggesting that part of the signal may originate from enhancement of the antiferromagnetic coupling between local $L1_0$ domains.

This heterogeneous description of the structure must be reconciled with the earlier report that did not find $L1_0$ nucleation sites by either diffraction or magnetic measurements.[14] These two sets of experiments were performed on different sets of samples; relatively thick films that differed in the substrate deposition temperatures for the EXAFS and thin films of varying thickness that were given a thorough annealing for the diffraction. It could be expected that the former procedure would promote larger numbers of $L1_0$ domains as the more mobile atoms find more stable residences in many smaller domains whose size is constrained by the brief interval before they are enveloped by the growing film. The major difference, however, may be equating magnetically ordered $L1_0$ nanodomains with nucleation sites that not only will all seed the large $L1_0$ domains in the homogeneous polycrystalline films after annealing but also are the limiting factor in this growth. The diminution or absence of the signature of the $L1_0$ phase in diffraction patterns and the EXAFS results indicating high but still partial ordering and residual strain in the locally $L1_0$ structured regions imply an aperiodic and out-of-registry arrangement of $L1_0$ domains with sizes at and below the diffraction limit. The $L1_0$ structure will then develop fully as much by the linking and merging of these nanodomains that originally incorporate a large fraction of the material as much as by their growth. Although this contradicts much of the dogma on transformations, the conventional approach to such transitions was based on crystallographic data and concepts, and we have observed extensive local complexity in several systems, for example, PuGa.[24]

Finally, we have the phase shift result indicating that the short-range coherent fraction of the material that is the site of the spin ordering undergoes a continuous change in the structure of its more distant component shells rather than being rigidly locked in the end point structure. This has been discussed in the context of the modeling and has been shown to reflect the domain size and possible dislocation-induced stabilization for large domains that destroys the coherence between them. The significance of this in terms of properties is that it is suggests

that the magnetic properties are initiated prior to full ordering and that the ordering of the spins from the individual atoms on the chemically ordered NiMn lattice is likely to be more important in creating this effect than the structural effect of the tetragonal distortion. The magnetism can therefore occur in the coherent structures, which are characterized by smaller domains.

V. Conclusions

We have reported on Mn *K*-edge XAFS measurements of thin films of NiMn. The data were interpreted in combination with XRD results that provide information on long-range order. The results reveal that the films are inhomogeneous or heterogeneous on atomic to nanometer length scales. Though we have not established the uniqueness of the structural solution, the local structure can be understood as a mixture of tetragonal $L1_0$ nanodomains with typical size greater than 5−6 Å but smaller than the diffraction limit, in combination with similar large domains that average to the chemically disordered fcc phase and with a significant disordered component that is the interface between these two structures or between incoherent $L1_0$ domains. From both the 2S fit and group fits of the extended structure supplemented by a qualitative phase shift analysis of the third to fifth shell contribution, the S_{SRO} parameter increases with increase of the growth temperature. S_{SRO} is substantial even in films grown at only 3 °C, indicating that small domains of the (crystallographic) $L1_0$ phase form before the signature of this phase appears in the diffraction patterns. Comparing the amount of $L1_0$ domains with exchange coupling values demonstrates that the observed magnetic behavior can be attributed to the presence of nano- and subsequently larger domains of antiferromagnetic, chemically ordered $L1_0$ phase. We have also examined the ordering process on the nanoscale and its effect on the structure and signature in diffraction patterns. In coherent structures, diffraction patterns overlook the presence of nanoscale clusters and reveal instead an average higher-symmetry structure. Incoherent structures with dislocations at the interfaces of domains can provide significant stress relief within each domain, and the diffraction patterns show coexisting structures as a result. This suggests that magnetic order is probably more correlated with the $L1_0$ chemical ordering than the tetragonal distortions in NiMn. The study of the electronic and magnetic properties of such domains embedded in a chemically disordered fcc matrix is described in the next paper of this series.

Acknowledgment. This work was supported by DOE OBES Division of Chemical Sciences under Contract W-7405. XAFS measurements were performed at SSRL (Stanford Linear Accelerator Center) and NSLS (Brookhaven National Laboratory), which are operated by the U.S. Department of Energy, Office of Basic Energy Sciences. This work was partially performed under the auspices of the U.S. DOE, Division of Materials Science, Office of Basic Energy Sciences, under contract DE-AC02-76CH00016.

References and Notes

(1) Cho, A. *Science* **2002**, *295*, 1992.
(2) Moreo, A.; Yunoki, S.; Dagotto, E. *Science* **1999**, *283*, 2034.
(3) Conradson, S. D.; Espinosa, F. J.; Henderson, A.; Villella, P. M. In *Physics in Local Lattice Distortions*; AIP Conference Proceedings 554; Oyanagi, H., Bianconi, A., Eds.; American Institute of Physics: Melville, NY, 2001; p 503.
(4) *Landolt-Bornstein New Series*; Hellwege, K. H., Ed.; Springer-Verlag: Berlin, 1971; Vol. 6, p 731.
(5) Nogues, J.; Schuller, I. K. *J. Magn. Magn. Mater*. **1999**, *192*, 203.
(6) Devasahayan, A. J.; Kryder, M. K. *IEEE Trans. Magn*. **1999**, *35*, 649.
(7) Lin, T.; Mauri, D.; Staud, N.; Huang, C.; Howard, J. K.; Gorman, G. L. *Appl. Phys. Lett*. **1994**, *65*, 1183.
(8) Mao, S.; Gangopadhyay, S.; Amin, N.; Murdock, E. *Appl. Phys. Lett*. **1996**, *69*, 3593.
(9) Schonfeld, B. *Prog. Mater. Sci*. **1999**, *44*, 435.
(10) Anderson, G. W.; Huai, Y.; Pakala, M. *J. Appl. Phys*. **2000**, *87*, 5726.
(11) Zhang, Y. B.; van der Heijden, P. A. A.; Nozieres, J. P.; Pentek, K.; Chin, T. K.; Tuchscherer, T.; Zeltzer, A. M.; Blank, H. R.; Trotter, S.; Jaren, S.; Speriosu, V. S. *IEEE Trans. Magn*. **2000**, *36*, 586.
(12) Garcia-Adeva, A. J.; Conradson, D. R.; Villella, P.; Conradson, S. D. *J. Phys. Chem. B* **2003**, *107*, 6704.
(13) Bishop, A. R.; Lookman, T.; Saxena, A.; Shenoy, S. R. *Europhys. Lett*. **2003**, *63*, 289.
(14) Toney, M. F.; Samant, M. G.; Lin, T.; Mauri, D. *Appl Phys. Lett*. **2002**, *81*, 4565.
(15) Warren, B. E. *X-Ray Diffraction*; Dover: New York, 1969.
(16) Lawson, A. C.; Martinez, B.; Von Dreele, R. B.; Roberts, J. A.; Sheldon, R. I.; Brun, T. O.; Richardson, J. W., Jr. *Philos. Mag. B* **2000**, *80*, 1869.
(17) Teo, B. K. In *EXAFS: Basic Principles and Data Analysis*; Springer-Verlag: Berlin, 1986.
(18) Stern, E. A. *Phys. Rev. B* **1993**, *48*, 9825.
(19) Zabinsky, S. I.; Rehr, J. J.; Ankudinov, A.; Albers, R. C.; Eller, M. J. *Phys. Rev. B* **1995**, *52*, 2995.
(20) This principle is known as the phase transferability. However, using the phase shift from the standard sample should be avoided if the primary purpose of XAFS analysis is to reconstruct genuine PDF or to trace driving forces for the local distortions.
(21) Cebollada, A.; Weller, D.; Sticht, J.; Harp, G. R.; Farrow, R. F. C.; Marks, R. F.; Savoy, R.; Scott, J. C. *Phys. Rev. B* **1994**, *50*, 3419.
(22) Dimitrov, D. A.; Ankudinov, A. L.; Bishop, A. R.; Conradson, S. D. *Phys. Rev. B* **1998**, *58*, 14227.
(23) It is a limitation of the conventional XAFS analysis that it provides the pair distribution function but not a 3D picture of the cluster about the absorption site.
(24) Conradson, S. D. *Appl. Spectrosc*. **1998**, *52*, A252.
(25) Withers, R. L.; Proffen, Th.; Welberry, T. R. *Philos. Mag. A* **1999**, *79*, 753.
(26) Warren, B. E. *X-Ray Diffraction*; Dover: New York, 1990.
(27) Welberry, T. R.; Butler, B. D. *Chem. Rev*. **1995**, *95*, 2369.
(28) Welberry, T. R.; Butler, B. D. *J. Appl. Crystallogr*. **1994**, *27*, 205.
(29) Garcia-Adeva, A. J.; Conradson, D. R.; Villella, P.; Conradson, S. D. *J. Phys. Chem. B* **2003**, 6704.
(30) Rose, J. H.; Smith, J. R.; Guinea, F.; Ferrante, J. *Phys. Rev. B* **1984**, *29*, 6.